

Collection of reciprocal space maps using imaging plates at the Australian National Beamline Facility at the Photon Factory

S. T. Mudie,^{a*} K. M. Pavlov,^a M. J. Morgan,^a
J. R. Hester,^b M. Tabuchi^c and Y. Takeda^c

^a*School of Physics and Materials Engineering, Monash University, Victoria 3800, Australia,* ^b*Australian Nuclear Science and Technology Organisation, PMB 1, Menai, NSW 2234, Australia,* and ^c*Department of Materials Science and Engineering, Graduate School of Engineering, Nagoya University, Nagoya 464-8603, Japan.*
E-mail: stephen.mudie@spme.monash.edu.au

Weissenberg screens and a translating cassette have been employed to allow an imaging plate to collect 30 scans per readout. In this configuration the imaging plate functions as a curved one-dimensional position-sensitive detector and, by changing the sample angle for each of the scans, two-dimensional images were produced in reciprocal space. This method of data collection leads to a reduction in scan time compared with methods based on a scintillation detector, particularly for asymmetric reflections. The data-collection method was tested using InGaN/GaN/AlN multilayers on sapphire substrates, since these exhibit broad features in reciprocal space. The geometry of the scans in reciprocal space required the data to be interpolated onto a Cartesian grid. Several interpolation schemes were investigated, with the results compared with the reciprocal space maps collected using a triple-axis scheme with a point detector. The quality of the interpolated reciprocal space maps depends upon the size and shape of the feature in reciprocal space, the interpolation method used, and the step size of the sample rotation. The method can be extended to three dimensions without an increase in data-collection time.

Keywords: reciprocal space maps; high-resolution X-ray diffraction; triple-axis diffraction; imaging plates; position-sensitive detectors.

1. Introduction

Synchrotron radiation is used to non-destructively characterize semiconductor heterostructures that are an integral part of advanced technology. In particular, X-ray diffraction provides important information about the quality and structure of semiconductor materials, ranging from those composed of several layers with varying composition to very complex multilayer structures, such as quantum dots, wires and superstructures (Fewster, 1997). The advantage of using synchrotron radiation derives from its high flux. However, even with large flux, it can still take many hours to investigate the region about a single reciprocal lattice point (RLP) as the layers are often thin (nanometres to micrometres) and/or of low crystalline quality. Since synchrotron beam time is limited, it is desirable to find ways of decreasing the time required to collect reciprocal space maps (RSMs), particularly as semiconductor structures become more complex and require more detailed experimental data for full characterization. Experimentally, it is necessary to examine a large region of reciprocal space to determine Bragg peak positions and intensities. However, to elucidate fine structure in the diffracted intensity

requires that small regions of reciprocal space be mapped at high resolution about many RLPs.

Currently, point detectors (*e.g.* scintillation counters) and area detectors (CCDs, imaging plates and film) are used for diffraction experiments. When coupled with high-precision rotation stages and high-quality analyser crystals in the triple-axis diffractometry (TAD) scheme (Iida & Kohra, 1979; Fewster, 1997; Holý *et al.*, 1999), point detectors offer large dynamic range, ease of data extraction, flexibility and very high angular resolution (several arcseconds). However, data-collection rates are low because the sample and/or analyser/detector position needs to be changed for each datum point. Position-sensitive detector (PSD) schemes overcome this problem by sampling extended areas of reciprocal space simultaneously. Unfortunately these detectors have poorer spatial resolution, dynamic range and signal-to-noise ratio than point detectors. Further, the analyser crystal discriminates intensity based on angle, whereas a PSD cannot distinguish between beams striking the detector at the same position but from different angles (and hence from different parts of the sample).

Selection of the detector and the diffractometer arrangement depends on the sample type. Semiconductor heterostructures are often grown as layers on thick highly crystalline substrates, which requires Bragg diffraction geometry and a detector robust enough to handle high-intensity beams diffracted from the substrate or thick high-crystalline layers, while still being capable of measuring low-intensity diffraction from thin layers. Since the individual layers are often of high crystalline quality the diffraction distribution exhibits fine structure, which should be measured with a high angular resolution. Therefore RSMs of semiconductor heterostructures have been routinely acquired using TAD because of the resolution and dynamic range characteristics (Fewster, 1997; Holý *et al.*, 1999).

As mentioned above the TAD method is slow, hence PSDs have been used for the collection of RSMs that may be applicable to characterizing semiconductor heterostructures. Gerhard *et al.* (2000) utilized a method whereby a ZnSe-based laser diode structure is illuminated by a highly divergent X-ray beam (from a synchrotron microfocus beamline). The diffracted intensity pattern is recorded on an imaging plate (IP). The incident-beam divergence is equivalent to rocking the sample during exposure to plane-wave irradiation. This method is very fast and simple, although the spot size used is small (10 μm) to achieve the greatest incident wavevector range possible. A small spot size avoids the various wavevectors being separated spatially. Hence this method collects information from a very small region of the sample, which can be an advantage or disadvantage depending upon the sample and the information required. A disadvantage of collecting a range of incident wavevector angles simultaneously is the integration of diffuse intensity within reciprocal space. The integration length depends directly on the range of wavevectors utilized. Gerhard *et al.* (2000) used a small wavevector distribution range, and so avoided excessive integration. If wide scans are required then it is necessary to use point (or one-dimensional) detectors to avoid integration over a large region of reciprocal space. Since one-dimensional detectors have a finite size they will also integrate along one reciprocal space direction. However, the integration is not affected by the angular range of the scan. The range of the integration can be reduced by using suitable slits to decrease the angular acceptance of the detector perpendicular to the diffraction plane.

A number of authors (Kinne *et al.*, 1998; Butler *et al.*, 2000; Welberry *et al.*, 2003) have used IPs as one-dimensional detectors. Weissenberg slits have been employed to mask the IP, which is translated perpendicular to the plane of diffraction. Kinne *et al.*

(1998) and Butler *et al.* (2000) report the collection of RSM data acquired by translating the IP and rotating the sample simultaneously to fill the entire detector area. Welberry *et al.* (2003) use a similar procedure except that the IP is stationary while being exposed. They have collected up to 300 strips, each 0.5 mm wide, on one imaging plate. Of these authors only Kinne *et al.* (1998) studied epitaxial layers on substrates, the sample type in which we are interested, using an IP detector in a one-dimensional mode. Butler *et al.* (2000) and Welberry *et al.* (2003) studied small single crystals. These systems are simple to set up compared with TAD, use a widely available PSD (IPs), and have a reasonable resolution and dynamic range. The level of integration within reciprocal space is dependent upon the slit width and can be made quite small. Each of these methods require angular calibration of the image plates (Kinne *et al.*, 1998; Butler *et al.*, 2000; Welberry *et al.*, 2003). This was carried out using high-intensity well known reflections from the sample. Welberry *et al.* (2003) also required a calibration to account for the decay in the recorded intensity with time over the duration of the scan.

Osborn & Welberry (1990) and Boule *et al.* (2002) both describe curved one-dimensional position-sensitive wire (or blade) detectors, which allow many scans to be collected without the need to change film or imaging plate. Although these detector systems allow high resolution to be achieved, they are expensive and can be damaged by synchrotron beam intensities. This is particularly true for samples that exhibit strong substrate reflections. Hence, despite their advantages, these detectors are not suited to our experimental work, which uses synchrotron radiation to investigate epitaxial layers grown on substrates.

Owing to the advantages outlined above, we used IPs and Weissenberg slits to collect RSMs. Unlike Kinne *et al.* (1998) we performed our experiments at a synchrotron facility. In contrast to Kinne *et al.* (1998), Butler *et al.* (2000) and Welberry *et al.* (2003), we compare the results obtained with IPs to RSMs collected in a high-resolution (TAD) mode using a point detector, and outline the interpolation methods used. In brief, the organization of this paper is as follows. In §2 we outline the mathematical relationship between angular (real) space and reciprocal space, and detail the experiment where RSMs were collected using IPs. §3 presents the results from the experiment, with a discussion in §4.

2. Experiment

For clarity we begin by describing the geometry of the IP and TAD methods in detail. Fig. 1 shows the experimental arrangement used to collect RSMs in the TAD scheme. Figs. 2(a) and 2(b) show the detailed diffraction geometry for angular and reciprocal space. The angle designations are the same as those used by Nesterets & Punegov (2000), where ω and ω' are the angular deviations (from the appropriate Bragg conditions) of the incident and diffracted waves,

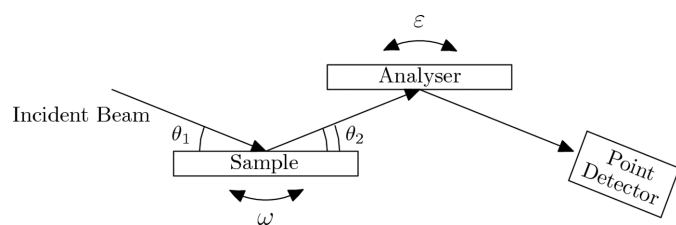


Figure 1
Geometry used in triple-axis diffractometry (TAD) to collect high-resolution RSMs. In a variant of the TAD scheme the detector is placed (with a narrow slit in front of it) perpendicular to the diffracted beam.

respectively, and ε is the angular deviation of the diffracted beam from the initial Bragg condition for the analyser. The angle between the surface of the sample and the diffraction planes (asymmetry angle) is specified by φ . The vectors \mathbf{k}_0 and \mathbf{k}_h are the incident and diffracted wavevectors, with magnitude $k = 2\pi/\lambda$; \mathbf{q}_x and \mathbf{q}_z are the reciprocal space vectors in the x and z directions, respectively, as shown in Fig. 2(b). The angles are related *via* the following equations,

$$\theta_1 \cong \theta_B - \varphi, \tag{1}$$

$$\theta_2 \cong \theta_B + \varphi, \tag{2}$$

$$\omega = (\varepsilon/2) + \Delta\omega. \tag{3}$$

The definition of (3) is applied such that $\Delta\omega$ specifies the deviation from the θ - 2θ scan. The reciprocal space diagram in Fig. 2(b) can be produced from Fig. 2(a) by rotating the coordinate system until the sample surface is horizontal. This is equivalent to a rotation angle of $\omega + \theta_B - \varphi$. Hence the angle between the \mathbf{q}_x axis and the direction to the detector slit position (or the middle of the angular window of the analyser crystal) is given by

$$\omega' + \theta_2 = 2\theta_B + \varepsilon - (\omega + \theta_B - \varphi) \tag{4}$$

$$= \theta_2 + \varepsilon - \omega, \tag{5}$$

and hence

$$\omega' = \varepsilon - \omega. \tag{6}$$

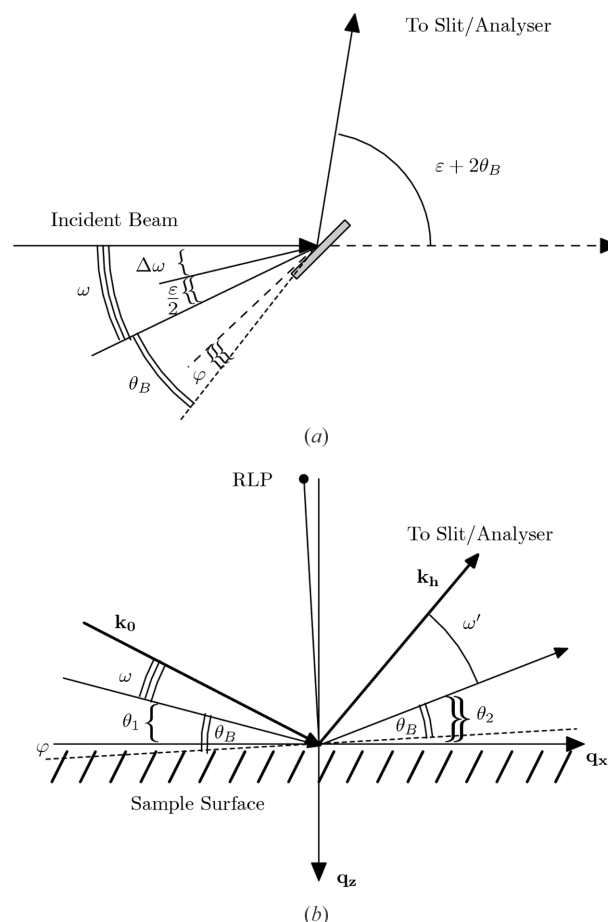


Figure 2
Angle definitions for scans in (a) angular space and (b) reciprocal space.

The following equations are used to convert from angular space to reciprocal space, assuming small deviations from the Bragg condition (Nesterets & Punegov, 2000),

$$\mathbf{q}_x = 2k\Delta\omega \sin \theta_B \cos \varphi - k\varepsilon \cos \theta_B \sin \varphi, \quad (7)$$

$$\mathbf{q}_z = -2k\Delta\omega \sin \theta_B \sin \varphi - k\varepsilon \cos \theta_B \cos \varphi. \quad (8)$$

For a symmetric reflection ($\varphi = 0$), \mathbf{q}_x is parallel to the $\Delta\omega$ axis for small values of $\Delta\omega$, and \mathbf{q}_z is antiparallel to the $\varepsilon/2$ axis (see Fig. 3*b*).

Replacing the analyser crystal and the point detector in Figs. 1 and 2 with a one-dimensional PSD, and keeping ω constant, the intensity is now recorded along a circular arc in reciprocal space as shown in Fig. 3*a*). A curved two-dimensional map in reciprocal space is produced by collecting data from the PSD for several ω positions. If the small-angle approximation is valid then the map is not curved, and equation (3) can be rearranged to give

$$\Delta\omega = \omega - (\varepsilon/2). \quad (9)$$

For constant ω the coordinate along the PSD is linear in ε ; in $(\varepsilon/2)-\Delta\omega$ space the PSD produces scans at 45° to the $\varepsilon/2$ axis, with intercept ω (see Fig. 3*b*). No assumptions have been made about the size of ω or ε , hence the $(\varepsilon/2)-\Delta\omega$ representation is useful for avoiding otherwise curved scans in $\mathbf{q}_x-\mathbf{q}_z$ space when the ω and ε ranges are large. It is particularly important for the interpolation described in §3.

Having described the geometry we now move to the particulars of the actual experiment. All experimental work was performed at the

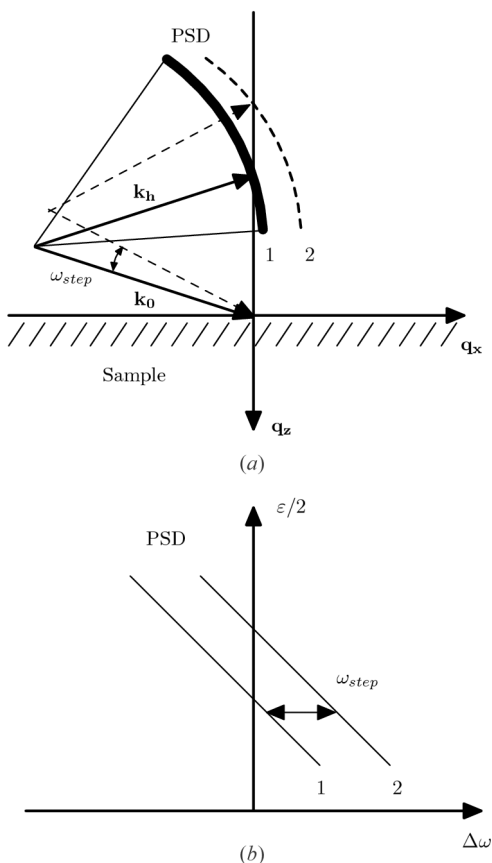


Figure 3 Symmetric reflection with a position-sensitive detector in (a) reciprocal space and (b) angular space. 1 and 2 indicate two different ω positions of the sample, and show how the position-sensitive detector covers reciprocal space to produce an RSM.

Australian National Beamline Facility (ANBF) on beamline 20B, at the Photon Factory, Tsukuba, Japan. The bending-magnet source delivers radiation from 4 keV to 25 keV ($\sim 3-0.05 \text{ \AA}$), with a Si(111) channel-cut monochromator selecting the desired energy. The monochromator can be de-tuned to reject higher harmonics.

The experimental hutch contains a large diffractometer (Barnea *et al.*, 1992; Garrett *et al.*, 1995) which can be evacuated to 0.01 torr in about 20 min. It houses a Huber 410 goniometer (ω) and a Huber 420 rotation arm (2θ), which are mounted coaxially with the axis of rotation horizontal. The IP cassette is centred on the ω goniometer, with radius 0.573 m, and covers $\pm 160^\circ$ in 2θ . The capacity of the cassette is eight $400 \text{ mm} \times 200 \text{ mm}$ IPs, with the long side oriented along the circumference. Radioactive fiducial markers are installed in the cassette to provide an angular standard on the IP. Weissenberg screens can be installed so that only 4 mm of the plate is exposed at one time. The IP cassette can be translated perpendicular to the plane of diffraction (see Fig. 4) so that up to 30 exposures can be collected on one plate, with a 1.5 mm gap between each exposed strip. The rotation stages, IP cassette, slits and detectors are computer controlled.

The IPs were scanned using a Fuji Film BAS2000 system, which provides a dynamic range of 10^4 and an effective spatial resolution of $100 \mu\text{m}$. This resolution equates to an angular resolution of 0.01° in 2θ . Software written in-house at the ANBF is available for angular calibration of the IP using the fiducial marks, plate-rotation correction and for extracting individual strips from the scan. A high-count-rate scintillation detector (Radicon) is used for double- and triple-axis diffractometry.

The samples investigated in this experiment were InGaN/GaN($2 \mu\text{m}$)/AlN(30 nm) multilayers grown on sapphire substrates. The AlN and GaN layers serve as buffers between the optoelectronically active InGaN layer and the lattice mismatched sapphire substrate. Three InGaN compositions ($\text{In}_{0.3}\text{Ga}_{0.7}\text{N}$, $\text{In}_{0.05}\text{Ga}_{0.95}\text{N}$ and $\text{In}_{0.42}\text{Ga}_{0.58}\text{N}$) were used. The 5% In layer was 200 nm thick and the other two layers were 20 nm thick. We have studied these samples at the ANBF previously (Mudie *et al.*, 2002, 2003), using a scintillation detector for the collection of the RSMs in the TAD scheme. Although high-resolution RSMs were collected in these earlier experiments, data acquisition was time-consuming. We have therefore employed a low-resolution scheme using a PSD, which is less time-demanding than TAD. The low-resolution scheme can be used for our samples because they exhibit no fine structure in the RSMs.

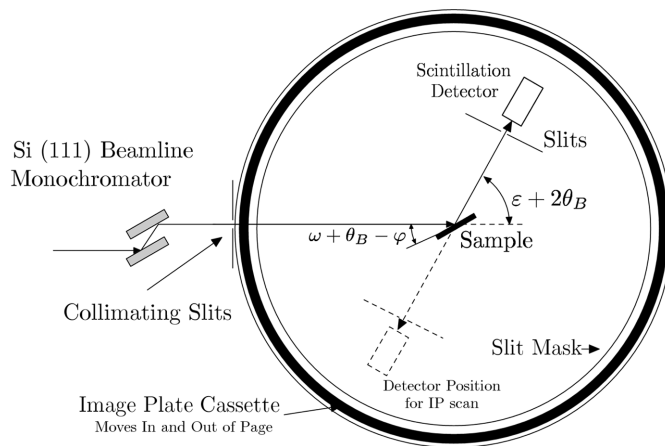


Figure 4 Diffractometer configuration (side view) showing the location of the IP cassette.

An incident wavelength of 1.54 \AA was selected and the monochromator was de-tuned to reject higher-order harmonics. The diffractometer entrance slits were adjusted to $4 \text{ mm} \times 0.1 \text{ mm}$ (width \times height). This matched the beam to the width of the IP strips, and to the spatial resolution of the IP. The sample stage was mounted on the ω goniometer and the scintillation detector and slits were mounted on the 2θ arm. This configuration is shown schematically in Fig. 4.

The scintillation detector was used to align the sample and to collect an RSM using the TAD scheme (see Fig. 1 and caption); a 0.5 mm -wide slit was used in front of the detector. The TAD RSM was subsequently compared with RSMs collected using the IPs. The detector was rotated to the bottom of the diffractometer during IP collection, as indicated in Fig. 4, so as not to obscure the synchrotron beam. The diffractometer was evacuated for the collection of all RSMs to reduce air scatter.

The first strip on each IP was reserved for a crystal truncation rod (CTR) scan [see Takeda & Tabuchi (2002) and references therein]. The CTR scan was collected by rotating the sample over the angular region of interest, including the nearest substrate peak, pausing for 1 s at each ω position to expose the IP strip. The CTR was used to confirm the correct angular calibration of the plate. As only one IP was used to collect an RSM, the number of ω positions was restricted to 29, and the 2θ angular range to 40° . The 2θ angular range is superfluous, but was set by the IP size. To increase the number of ω positions the IP would need to have been changed every 29 scans. Although this is possible, it would require the diffractometer to be evacuated each time, significantly increasing the time required to collect the RSM.

A software script was written by the authors to control the ω stage, the IP cassette and the shutter during collection of RSMs. Initially the exposure time was varied to determine a suitable value for our samples. Using the highest sensitivity on the scanner, a time of 45 s per strip avoided overexposing the peak due to the thick 2 \mu m GaN layer, while being long enough to collect peaks originating from the thin $20\text{--}200 \text{ nm}$ InGaN layer.

3. Results

Fig. 5 shows a section of an ‘as collected’ IP for the $\text{In}_{0.3}\text{Ga}_{0.7}\text{N}/\text{GaN}/\text{AlN}$ sample about the GaN(0004) reflection. The strips are clearly identifiable near the peaks; however, within each strip the peak intensity is not centred. This was corrected for later by varying the off-plane angle of the sample. The strip on the far left is the CTR and the bright spot on the extreme right is a fiducial mark. The IP scans were converted into 30 one-dimensional scans using in-house software. The software calibrated the ε axis using the fiducial marks, then integrated in the ω direction across each scan to obtain the intensity.

The unprocessed data in Fig. 5 lie on a regular two-dimensional Cartesian grid in ω –($\varepsilon/2$) space. We can move to $\Delta\omega$ –($\varepsilon/2$) space (see Fig. 6) using equation (9) [and then to \mathbf{q}_x – \mathbf{q}_z space using equations (7) and (8)]; however, the grid formed is not regular along the $\Delta\omega$ axis. In order to plot the RSMs and extract profiles along various directions, the data must be interpolated onto a regular (Cartesian) grid. A number of interpolation schemes were implemented; however, the simplest is to interpolate in the $\Delta\omega$ direction. A cubic spline interpolation was used, as it was easy to implement and matches the data smoothly.

Fig. 6 shows the geometry of an entire scan after the unprocessed data (shown in Fig. 5) has been transformed to angular coordinates $\Delta\omega$ –($\varepsilon/2$). Within reciprocal space the scan would be an arc (see Fig. 3a), because the small-angle approximation breaks down owing to the large angular range (*i.e.* 20° in $\varepsilon/2$).

Fig. 7 shows a comparison of an RSM acquired with an IP and the TAD scheme. The scans are about the GaN(0004) peak and encompass the $\text{In}_{0.3}\text{Ga}_{0.7}\text{N}$ (0004) peak. The line profiles have been extracted from the RSM, not collected separately. The background has been subtracted and the scans normalized to the InGaN peak height. The error plot (Fig. 7b) is given by

$$\text{RSM}_{\text{Error}} = \log_{10}(\text{RSM}_{\text{IP}}/\text{RSM}_{\text{TAD}}). \quad (10)$$

An IP scan was also collected with half the step size in the ω direction (see Fig. 8). Only one IP was used, which covered half the area of the RSM presented in Fig. 7. This results in the truncation seen in Fig. 8(a). The data-collection time was identical to the lower-resolution scan shown in Fig. 7.

In Fig. 7 the step size in the $\Delta\omega$ direction (as determined by the interpolation of the IP RSM) was matched to that used for the TAD technique. The small-angle approximation [equations (7) and (8)] was

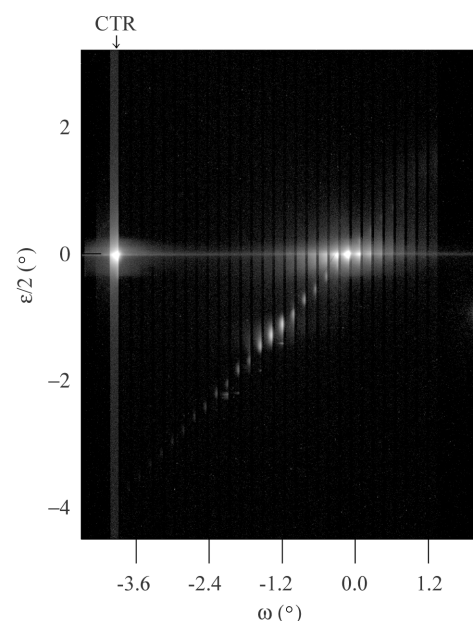


Figure 5 Section of an unprocessed imaging plate for the $\text{In}_{0.3}\text{Ga}_{0.7}\text{N}/\text{GaN}/\text{AlN}$ sample about the (0004) reflection.

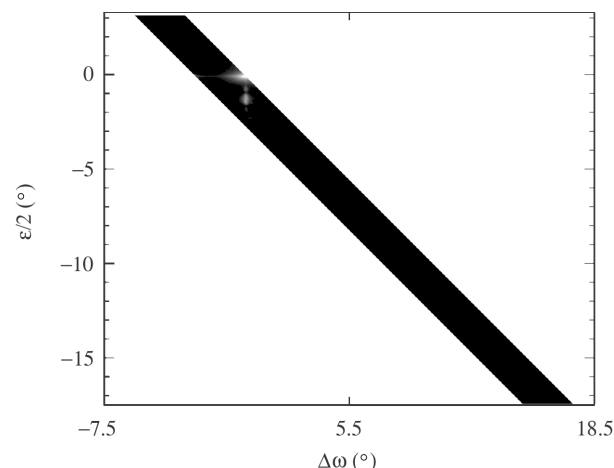


Figure 6 Entire RSM from a single imaging plate after cubic spline interpolation for the $\text{In}_{0.3}\text{Ga}_{0.7}\text{N}/\text{GaN}/\text{AlN}$ sample about the (0004) reflection.

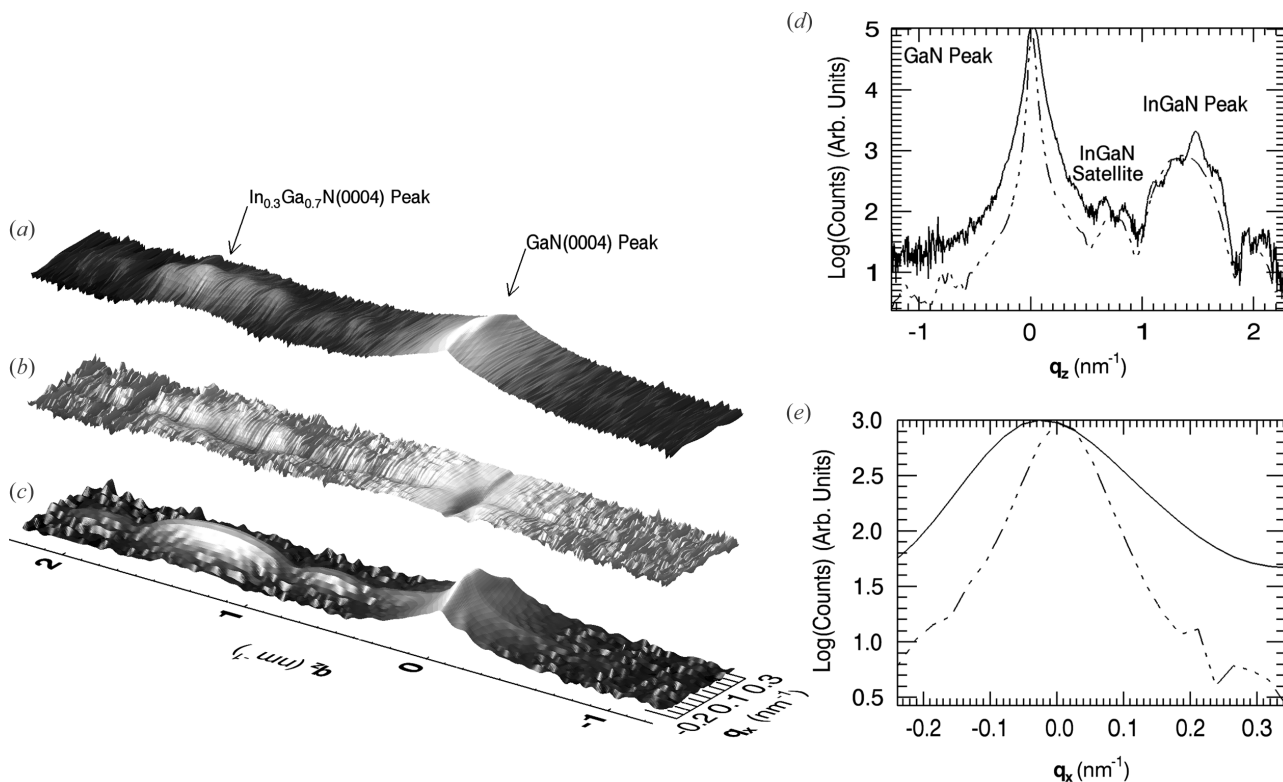


Figure 7
 Comparison of triple-axis RSM and interpolated IP data. (a) Interpolated IP RSM, (b) error plot, (c) triple-axis RSM, (d) ω - 2θ scan (extracted from RSM), and (e) ω scan (extracted from RSM). Note that a logarithmic vertical axis is used for each plot. Full line: IP method with interpolation. Dashed line: TAD technique.

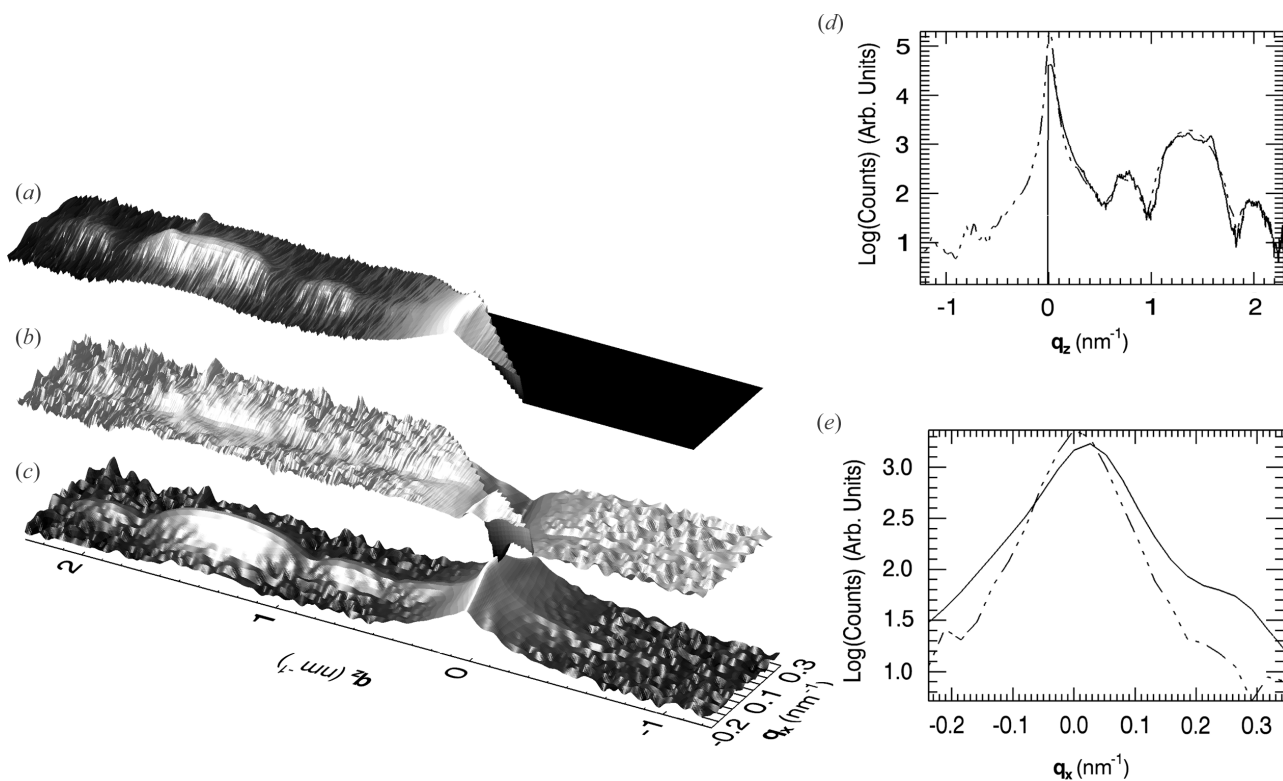


Figure 8
 Comparison of triple-axis RSM and interpolated high-resolution IP data. (a) Interpolated IP RSM, (b) error plot, (c) triple-axis RSM, (d) ω - 2θ scan (extracted from RSM), and (e) ω scan (extracted from RSM). Note that a logarithmic vertical axis is used for each plot. Full line: IP method with interpolation. Dashed line: TAD technique.

assumed in transforming from angular space $[\Delta\omega-(\varepsilon/2)]$ to reciprocal space to avoid further interpolation.

Fig. 9 shows two plots around the $(11\bar{2}4)$ reflection for different samples.

All interpolation and analysis was performed using software written in IDL 6.0 by the authors.

4. Discussion

The aim of this experiment was to utilize the IPs for collecting RSMs rapidly. Superficially the IP method appears attractive, since a scan can be acquired in approximately 45 min, which includes evacuation of the diffractometer chamber and readout of the IPs. A TAD scan, covering the same peak features, requires 3–4 h depending upon the region of interest and spatial resolution. However, before IPs are adopted for routine reciprocal space mapping, it is imperative to establish the suitability of the method for various scan types and to validate the accuracy of the RSM data obtained in the present experiments. These issues are addressed in the remainder of the paper.

Fig. 7 indicates that there are significant differences between the RSM data collected using the TAD method and the IP with interpolation. In particular, the peak is substantially widened in the ω direction (see Fig. 7e), and does not have the correct shape. The ω - 2θ scan, however, is more accurate, showing all features of the TAD RSM. This means that the IP method can be successfully used for producing ω - 2θ scans with an IP detector for Group III nitride multilayer samples. It is difficult to specify a resolution for the IP scans because the data are highly asymmetric. The spacing between collected lines (see Fig. 3b) in the $\Delta\omega$ direction (before interpolation), as determined by ω_{step} , is 0.18° for Fig. 7 and 0.09° for Fig. 8. However, along the lines (see Fig. 3b) the step size is up to 20 times smaller (*i.e.* 0.01°). Limiting ourselves to one IP has resulted in a low

spatial resolution compared with Kinne *et al.* (1998). The resolution could be increased, using only one IP, if the Weissenberg screens are made narrower and the IP cassette step size is reduced.

Fig. 8 shows that reducing the ω step size by a factor of two significantly improves the result, in both the q_x and q_z directions. This suggests that, for our sample type, 58 scans are sufficient to cover the range of interest. This should be easy to obtain with some minor modification to the IP system, namely slit and step sizes. The majority of the scan collection time is spent evacuating the system and handling/scanning the IPs. Hence an increase in the number of strips on one plate will not significantly change the scan collection time. Note that information on the IP degrades with time, and can require a correction as explained by Welberry *et al.* (2003). However, as we collected a small number of scans, and hence achieved fast IP throughput, this problem was avoided.

In attempting to cover an extended range in reciprocal space by using a large ω_{step} (see Fig. 3b), the interpolation procedure introduces false peaks. These can be seen in the InGaN peak, and its satellite in the ω - 2θ scan (see Fig. 7d). Fig. 10 shows a schematic illustration of this phenomenon for a peak elongated along the q_z direction (*e.g.* the InGaN peak). In Fig. 10(a) the data points lying on

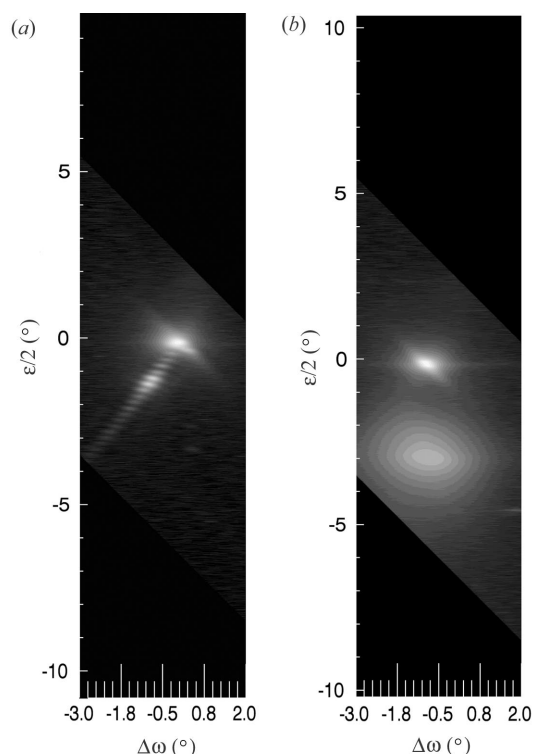


Figure 9
Plots of $(11\bar{2}4)$ reflections. Note that axes are in angular units.

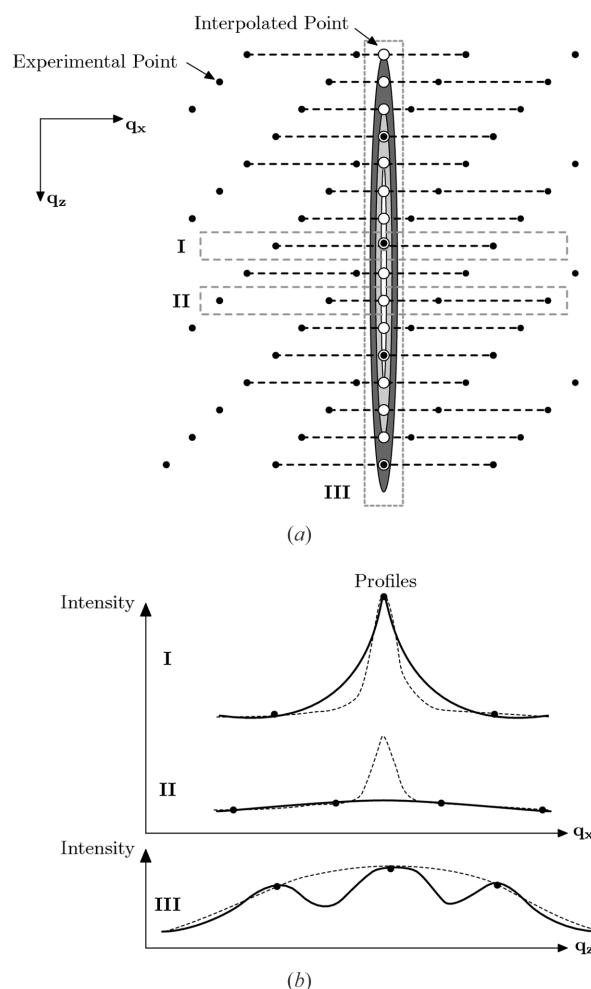


Figure 10
Schematic explaining the origin of peak splitting when ω_{step} is large. (a) Sketch of the RSM showing the position of the experimental (filled circles) and interpolated (open circles) points compared with the 'true' peak, and (b) profiles across the 'true' (dotted line) and interpolated (solid line) peaks, from regions I, II and III indicated in (a).

the peak are generated, *via* interpolation in the q_x direction, from widely spaced experimental points. In general, the experimental points straddle the peak position and hence give a result less than the true peak intensity. This situation is evident in region II in Fig. 10(a). A profile of this region is displayed in Fig. 10(b), which clearly indicates that the interpolated scan has a lower intensity than the true peak. Fig. 10(a) shows that the experimental points are arranged obliquely to the peak direction. Hence some experimental points lie closer to, or on, the peak leading to a more accurate peak intensity. This is the case for region I where an experimental point lies exactly on the peak. The resulting profile is shown in Fig. 10(b). Therefore a translation in the q_z direction produces a series of maxima as shown for region III. A similar problem arises for the GaN peak, which is elongated in the q_x direction, if interpolation is performed in the q_z direction. Therefore the result of interpolation depends on the geometry, and in particular the width of the peak being interpolated compared with the resolution (if a large ω_{step} is used).

Since no explicit smoothing has been applied (only that inherent in the interpolation scheme), further improvement may be possible through the application of suitable filtering; however, such a procedure would require careful justification.

The IP scans were collected in approximately one quarter of the time required for the TAD technique. Hence, subtracting every second row and column reduces the TAD RSM to one that would have been collected in approximately the same time as the IP scans. Fig. 11 compares the cross sections of the high- and low-resolution

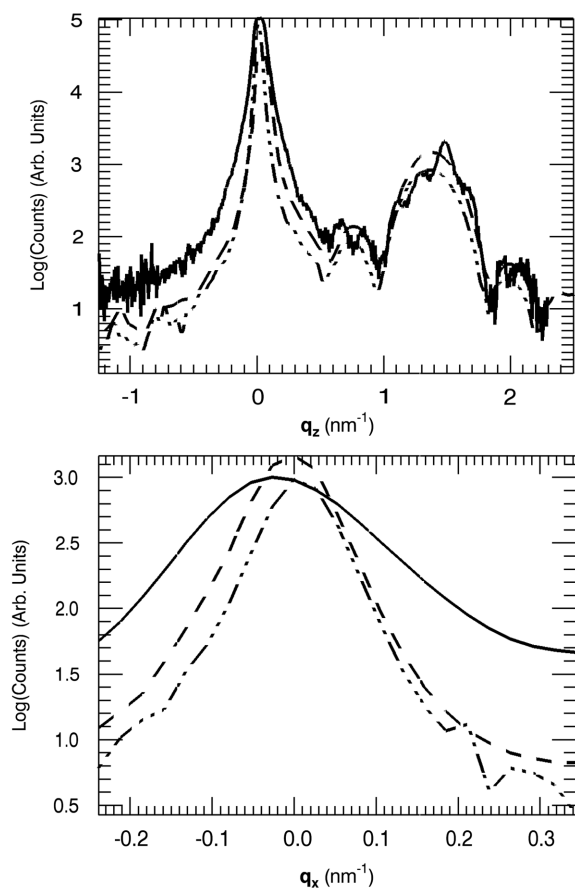


Figure 11
Comparison of RSMs obtained using an IP, TAD and the reduced TAD method. Full line: IP RSM. Dashed line: resized standard RSM. Dot-dashed line: full standard RSM.

TAD RSMs with the interpolated IP scans. The low-resolution TAD RSM was linearly interpolated onto the same grid size as the high-resolution RSM. Comparing the sparse TAD scan with the IP scan suggests that, for the region of interest, data of similar or better quality can be collected in a comparable time using the TAD method than with the IP method. The sparse TAD RSM is of a higher resolution than the IP RSM because the sample spacing is less asymmetric. However, the TAD method requires:

- (i) Greater time for set-up;
- (ii) *A priori* knowledge of the peak positions in reciprocal space. This is problematic for unknown samples, especially for asymmetric reflections (see Fig. 9) and requires long alignment times;
- (iii) More complicated instrumentation, such as a second axis of rotation for the detector/analyser.

The RSMs collected by the IP cover a much wider range than the specific region of interest shown in Fig. 7, although much of this extended region is featureless. However, there are specific cases where the large region can be useful. For example, Fig. 12 shows a scan where powder lines, possibly due to segregated In clusters, were observed across the entire RSM, simultaneously with the Bragg and diffuse peaks.

Fig. 9 shows two RSMs about $(11\bar{2}4)$. RSMs of asymmetric reflections must cover wide regions of reciprocal space, because the peaks do not necessarily align with the q_x or q_z axes. Hence the ability of the IP scans to cover a large region of reciprocal space in a short period of time is very useful for scanning asymmetric reflections (even with low resolution). The range along the $\Delta\omega$ axis shown in Fig. 9 is more than seven times wider than that shown for the symmetric reflection in Fig. 7.

We have introduced integration in the q_y direction by summing across the strips. Summing in the q_y direction over a small range can also introduce errors if the peaks in that direction have different widths. It may be more valid to use the central line of pixels from the strip, and hence remove any integration; however, this would require that the scan be centred correctly on the strip. The TAD method also integrates in the q_y direction (Holý *et al.*, 1999). Kinne *et al.* (1998) fill an entire IP by scanning it past a narrow slit, thereby avoiding the need to integrate in the q_y direction. However, we observed that very bright features caused streaks on the IP in the $\Delta\omega$ direction, presumably because of saturation. Increasing the gap between strips reduces the intensity of the streaks at the adjacent strip position on the IP. No such gaps exist for the procedure adopted by Kinne *et al.* (1998), although the lower count rate of the laboratory X-ray source

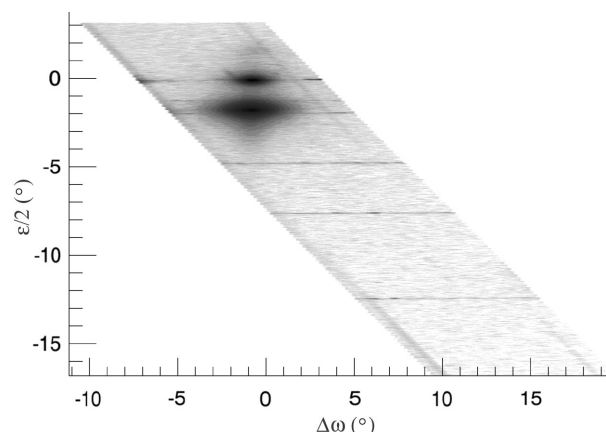


Figure 12
Powder lines collected across the whole imaging plate, possibly due to In segregation.

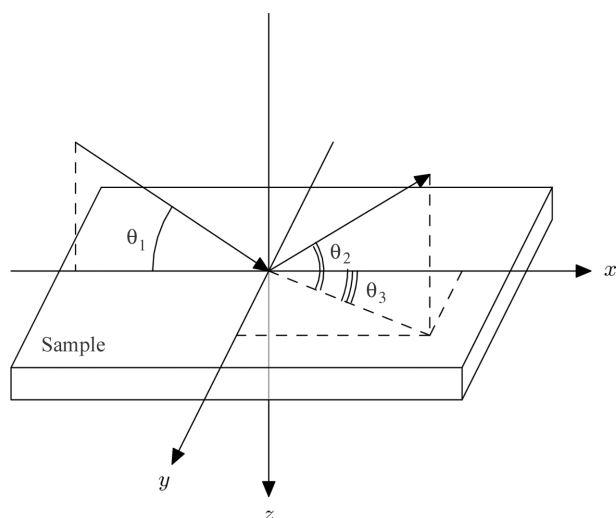


Figure 13
Angle designations for the three-dimensional diffraction geometry.

may have resulted in a less severe problem. The optimum detector for this collection regime would have digital on-line readout, such as that used by Boule *et al.* (2002), but be capable of handling synchrotron intensity, be vacuum stable, and have an appropriate dynamic range. Such detectors are not readily available.

Experimentally we integrate over a small range of reciprocal space, because of a number of instrumental effects (*e.g.* the slits are not infinitely narrow). If the Weissenberg slits were removed, the lateral direction would be available for detecting intensity. This direction corresponds to \mathbf{q}_y , which for an incident plane wave is given by

$$\mathbf{q}_y = \mathbf{k} \cos \theta_2 \sin \theta_3, \quad (11)$$

where θ_2 and θ_3 are defined in Fig. 13. [Note that equations (7) and (8) are not valid in the three-dimensional case.] Gerhard *et al.* (2000) use this fact to collect their RSMs. Their results are similar to a CTR scan (see *e.g.* Takeda & Tabuchi, 2002) with no Weissenberg slits installed. Such a CTR is still integrated over the \mathbf{q}_x range, determined by the ω limit selected, but now provides information from a two-dimensional region of reciprocal space. The CTR projects the three-dimensional RSM onto the \mathbf{q}_y – \mathbf{q}_z plane, *i.e.* perpendicular to the RSM. Hence, by collecting two-dimensional RSMs and two-dimensional CTRs, two perpendicular planes can be gathered without the need to rotate the sample about the \mathbf{q}_z axis between the two scans. This ensures that the same region of the sample is investigated for both the \mathbf{q}_y – \mathbf{q}_z and \mathbf{q}_x – \mathbf{q}_z planes.

If only a small \mathbf{q}_y range is required, and the incident beam has low angular divergence in both the \mathbf{q}_x and \mathbf{q}_y directions, then our technique can be used to produce a three-dimensional RSM. This is achieved by simply using the profile across the strips, instead of integrating. This cannot be easily achieved using other techniques, except for that of Welberry *et al.* (2003), although in this latter case it would have very limited range.

5. Conclusion

We have implemented a method for collecting reciprocal space maps using imaging plates at the Australian National Beamline Facility. The results indicate that for sparse data care must be taken when interpolating onto a regular grid. More specifically, peaks that are narrow in the \mathbf{q}_z direction should be interpolated in the \mathbf{q}_x direction, and *vice versa*, to avoid producing false peaks. For our sample type, and the range required, we found that as few as 58 strips can produce acceptable results. The IP method is very useful for scanning large areas when the peak position and shape are not known exactly, which occurs for asymmetric peaks; further, it does not require more sophisticated equipment, such as analyser crystals and 2θ arms. Significantly, sample features of interest may only be observed because of large angular range, such as powder peaks that suggests cluster segregation or polycrystalline regions.

This work was performed at the Australian National Beamline Facility with support from the Australian Synchrotron Research Program, which is funded by the Commonwealth of Australia under the Major National Research Facilities Program. The samples were prepared by Professors H. Amano and I. Akasaki at the Department of Materials Science and Engineering, Meijo University. The authors would like to thank Dr Imants Svalbe, Professor Rob Lewis, Dr Karen Siu and Professor Vasily Punegov for their valuable contributions. STM acknowledges the support of an Australian Postgraduate Award. KMP and MJM acknowledge the support of the Australian Research Council.

References

- Barnea, Z., Creagh, D. C., Davis, T. J., Garrett, R. F., Janky, S., Stevenson, A. W. & Wilkins, S. W. (1992). *Rev. Sci. Instrum.* **63**, 1069–1072.
- Boule, A., Masson, O., Guinebretière, R., Lecomte, A. & Dauger, A. (2002). *J. Appl. Cryst.* **35**, 606–614.
- Butler, B. D., Haefner, D. R., Lee, P. L. & Welberry, T. R. (2000). *J. Appl. Cryst.* **33**, 1046–1050.
- Fewster, P. F. (1997). *Crit. Rev. Solid State Mater. Sci.* **22**, 69–110.
- Garrett, R. F., Cookson, D. J., Foran, G. J., Sabine, T. M., Kennedy, B. J. & Wilkins, S. W. (1995). *Rev. Sci. Instrum.* **66**, 1351–1353.
- Gerhard, T., Albert, D. & Faschinger, W. (2000). *J. Cryst. Growth*, **214**, 1049–1053.
- Holy, V., Pietsch, U. & Baumbach, T. (1999). *High-Resolution X-ray Scattering from Thin Films and Multilayers*. Heidelberg: Springer-Verlag.
- Iida, A. & Kohra, K. (1979). *Phys. Status Solidi*, **51**, 533–542.
- Kinne, A., Thoms, M., Röss, H. R., Gerhard, T., Ehinger, M., Faschinger, W. & Landwehr, G. (1998). *J. Appl. Cryst.* **31**, 446–452.
- Mudie, S., Pavlov, K., Morgan, M., Tabuchi, M., Takeda, Y. & Hester, J. (2003). *Surf. Rev. Lett.* **10**, 513–517.
- Mudie, S. T., Pavlov, K. M., Morgan, M. J., Takeda, Y., Tabuchi, M. & Hester, J. R. (2002). *Proceedings of the 2002 Conference on Optoelectronic and Microelectronic Materials and Devices (COMMAD 2002)*, Sydney, Australia, 11–13 December 2002, pp. 111–116. Piscataway, NJ: IEEE.
- Nesterets, Y. & Punegov, V. (2000). *Acta Cryst.* **A56**, 540–548.
- Osborn, J. C. & Welberry, T. R. (1990). *J. Appl. Cryst.* **23**, 476–484.
- Takeda, Y. & Tabuchi, M. (2002). *J. Cryst. Growth*, **237/239**, 330–337.
- Welberry, T. R., Goossens, D. J., Haefner, D. R., Lee, P. L. & Almer, J. (2003). *J. Synchrotron Rad.* **10**, 284–286.